

OPTICAL AND UV SPECTRA OF THE REMNANT OF SN 1885 (S AND) IN M31<sup>1</sup>ROBERT A. FESEN<sup>2</sup>, KATHRYN E. WEIL<sup>2</sup>, PETER A. HÖFLICH<sup>3</sup>, AND ANDREW J. S. HAMILTON<sup>4</sup>*Submitted to the Astrophysical Journal*

## ABSTRACT

We present optical and ultraviolet spectra of Supernova 1885 (S And), visible in absorption against the bulge of the Andromeda galaxy (M31), taken with the Hubble Space Telescope STIS Spectrograph in order to probe the three dimensional arrangement of the supernova debris. Spectra covering 2900 – 5700 Å taken using six 0″.2 wide slit positions in two orientations show broad Ca II H & K absorption with blue and red radial velocities out to at least 11 500 km s<sup>−1</sup>, consistent with *HST* narrow passband Ca II images of S And. Enhanced Ca II absorption is seen between 2000 and 6000 km s<sup>−1</sup> suggestive of a Ca II-rich inner shell. The spectra also show strong, asymmetric Ca I 4227 Å absorption extending out to +12 400 km s<sup>−1</sup>, along with weak Fe I 3720 Å absorption apparently confined to a shell with expansion velocities between 2000 and 9000 km s<sup>−1</sup> on both the near and far sides of the remnant. Ultraviolet spectra obtained with a 0″.5 wide slit at one orientation revealed weak broad absorption shortward of 3000 Å consistent with model predictions. The STIS spectra, together with previous *HST* images, show a layered structure with a sharp and well defined Ca-rich outer edge indicative of a delayed detonation phase. The remnant’s clumpy inner Ca-rich shell plus only a handful of Fe-rich plumes is unlike morphologies expected from dynamical or violent merger scenarios. Instead, a small number of Fe-rich plumes suggest their formation during a deflagration phase by Rayleigh-Taylor instabilities but less well developed without extended mixing as expected from hydrodynamic calculations. The suppression of strong Rayleigh-Taylor instabilities is possibly the result of strong magnetic fields. As a likely scenario, we propose SN 1885 was an off-center, delayed detonation and slightly subluminous SN Ia event similar to SN 1986g.

*Subject headings:* supernovae: general - supernovae: individual (SN 1885) - ISM: kinematics and dynamics - ISM: abundances - supernova remnants

## 1. INTRODUCTION

Type Ia supernovae (SNe Ia) are thought to be the explosions of degenerate carbon-oxygen white dwarfs (WDs) that undergo a thermonuclear runaway when they reach the Chandrasekhar limit (Hoyle & Fowler 1960; Colgate & McKee 1969; Nomoto et al. 1984; Hillebrandt & Niemeyer 2000; Li et al. 2003). Possible SN Ia progenitor systems have been discussed recently by Howell (2011), Nugent et al. (2011), Bloom et al. (2012), Di Stefano & Kilic (2012), and Höflich et al. (2013).

Observed SNe Ia spectra and light curves suggest a layer structure with intermediate mass elements on the outside and nickel-iron material on the inside. Khokhlov (1991) proposed that SN Ia light curves could be explained empirically by a “delayed detonation transition” (DDT) scenario in which the explosion starts in the core as a burning deflagration wave, which is followed somehow by a detonation wave of overlying unburned material. The initial deflagration front pre-heats and expands the star’s outer layers. The consequence is the burning of the outer layers does not continue to completion and

a layered structure of intermediate mass elements is produced.

SN Ia explosions involve a complex interplay of turbulent hydrodynamics, nuclear burning, conduction, radiative transfer in iron-group rich material, and perhaps magnetic fields (Khokhlov 1995; Niemeyer & Hillebrandt 1995; Livne 1999; Reinecke et al. 1999; Gamezo et al. 2004; Röpke et al. 2012). This leads to significant uncertainties in the accuracy of the models. Several key questions about expansion asymmetries and the overall characteristics of SNe Ia could be resolved if one could obtain direct observations of the distribution and kinematics of elements in young SN Ia remnants.

The bright historical nova seen in 1885 known as S Andromeda (S And) located just 16″ away from M31’s nucleus offers an opportunity to study the expanding debris of a SN Ia. Because of its central location in M31, the remnant’s expanding ejecta is detectable not through line emission but via resonance line absorption against the background of the Andromeda galaxy’s bulge stars (Fig. 1; Fesen et al. 1989).

SN 1885 has been classified as a probable SN Ia as its reported optical spectrum lacked hydrogen lines, defining it as Type I (de Vaucouleurs & Corwin 1985). Its reddish appearance and fast light curve is consistent with subluminous Type Ia event (de Vaucouleurs & Corwin 1985) although this classification has been questioned (see Chevalier & Plait 1988; Pastorello et al. 2008; Perets et al. 2011).

Images taken with the Hubble Space Telescope (*HST*) revealed a circular  $\simeq 0″.75$  diameter dark spot pro-

<sup>1</sup> Based on observations with the NASA/ESA Hubble Space Telescope, obtained at the Space Telescope Science Institute, which is operated by the Association of Universities for Research in Astronomy, Inc. under NASA contract No. NAS5-26555.

<sup>2</sup> 6127 Wilder Lab, Department of Physics & Astronomy, Dartmouth College, Hanover, NH 03755

<sup>3</sup> Department of Physics, Florida State University, Tallahassee, FL 32306

<sup>4</sup> JILA and the Department of Astrophysical and Planetary Sciences, University of Colorado, Boulder, CO 80309

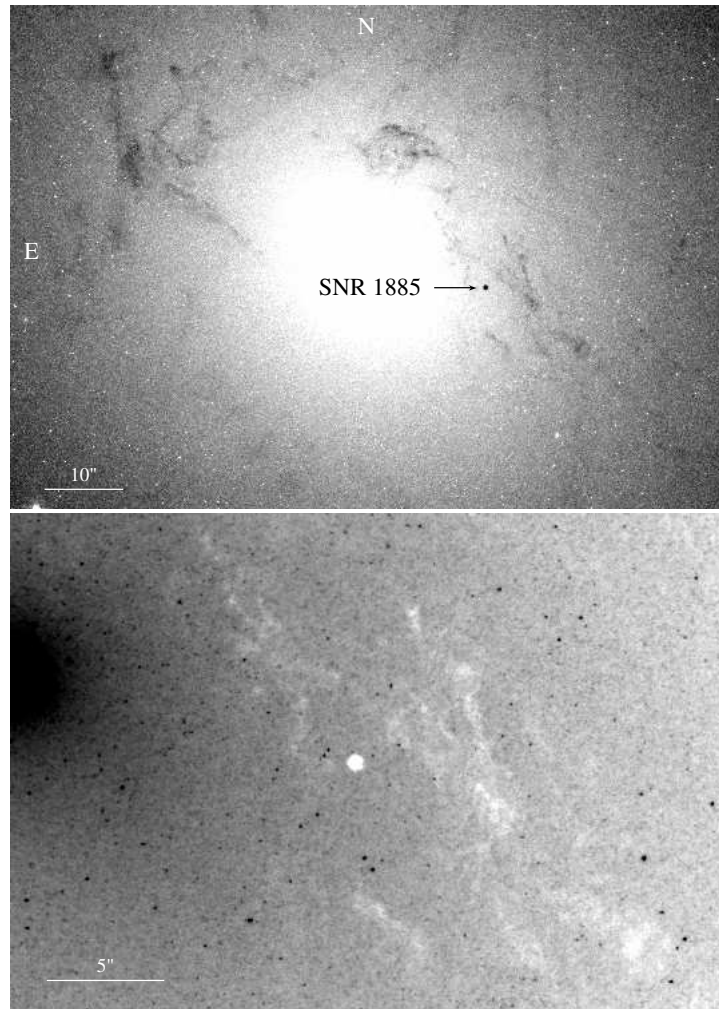


FIG. 1.— A December 2010 WFC3 image of the bulge of M31 taken with the F390M filter as part of an emission line mapping program of the nuclear regions of M31 (PI: Z. Li). A positive linear stretch of the M31 bulge is shown in the upper panel. The remnant of SN 1885 appears as a small ( $0.8''$ ) round dark spot of Ca II H & K absorption  $16''$  southwest of the nucleus. The bottom panel shows an enlarged section of this same image centered on the SN 1885 region but shown in a negative log stretch.

duced by a blend of Ca II H & K line absorption (Fesen et al. 1999). Subsequent ultraviolet imaging of the remnant with *HST* revealed a  $0''.5$  diameter absorption spot likely due largely to saturated UV Fe II resonance lines (Hamilton & Fesen 2000).

Spectra taken with Faint Object Spectrograph (FOS) on *HST* established that the absorption was produced principally by Ca II K & H  $3934, 3968 \text{ \AA}$ , with additional contributions from Ca I  $4227 \text{ \AA}$  and Fe I  $3441, 3720 \text{ \AA}$  (Fesen et al. 1999). The remnant’s Ca II absorption was found to extend to a velocity of  $\simeq 13\,100 \pm 1500 \text{ km s}^{-1}$ .

*HST* images taken in 2004 showed that the Ca II absorption is roughly spherical with a maximum diameter of  $0''.8$  (Fesen et al. 2007). At the known distance  $785 \pm 25 \text{ kpc}$  of M31 (McConnachie et al. 2005), this angular diameter corresponds to a mean expansion velocity of  $12\,500 \text{ km s}^{-1}$  over the  $\simeq 120 \text{ yr}$  age of SN 1885. The agreement between the remnant’s size and its expansion velocity as measured in the Ca II absorption implies that the SN 1885 remnant is still largely in free expansion. This is also consistent with the remnant being an exceptionally weak radio source (Sjouwerman & Dickel 2001;

Hofmann et al. 2013) with no confirmed associated X-ray emission (Kaaret 2002).

Additional *HST* images obtained in 2010 and 2012 show extended low velocity Fe I absorption slightly offset to the east from the remnant’s center as defined by Ca II images, likely due to an ionization effect caused by self-shielding (Fesen et al. 2015). More significant is the appearance of the remnant’s apparent Fe II distribution in a few streams or “plumes” of Fe-rich material extending out from the remnant’s center to  $\sim 10\,000 \text{ km s}^{-1}$ . This arrangement is in sharp contrast to the remnant’s Ca II absorption which extends out to  $12\,500 \text{ km s}^{-1}$  but is most concentrated in a clumpy shell spanning velocities of  $2000 - 5000 \text{ km s}^{-1}$ .

Because its ejecta are in free expansion, the distribution of elements in the remnant of SN 1885 (hereafter SNR 1885) is essentially the same as that shortly after the explosion. The dominant element near the center of the remnant at the present time is expected to be iron and the dominant iron ionization species is expected to be Fe II (see Fig. 2). The presence of Fe I in the FOS spectrum attests to the relatively low ionization state of the supernova ejecta in general more than a century af-



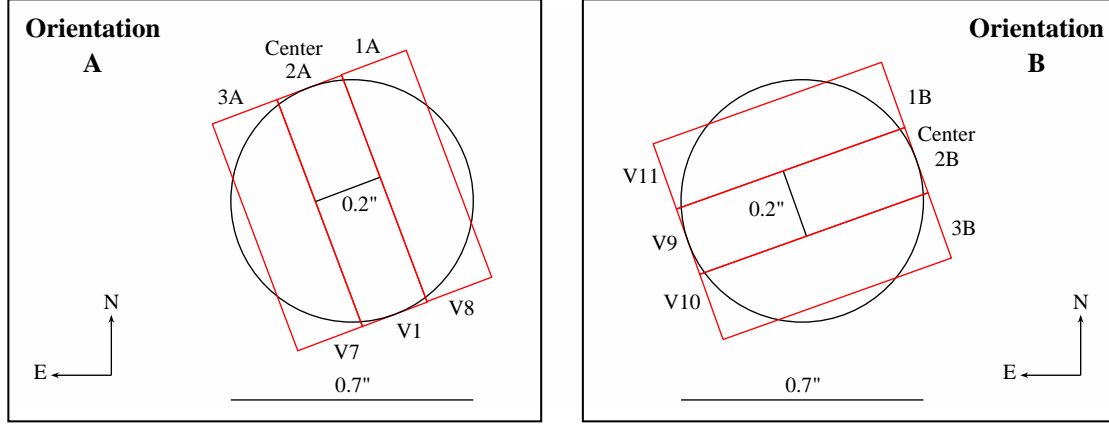


FIG. 3.— Diagram of the STIS/CCD slit positions for the observations of SNR 1885. Each slit was 0.2 arcseconds in width and 52 arcsecond in length. Circles are 0.7 arcseconds in diameter which corresponds to the approximate size of the remnant from the *HST* images presented in Fesen et al. (2015).

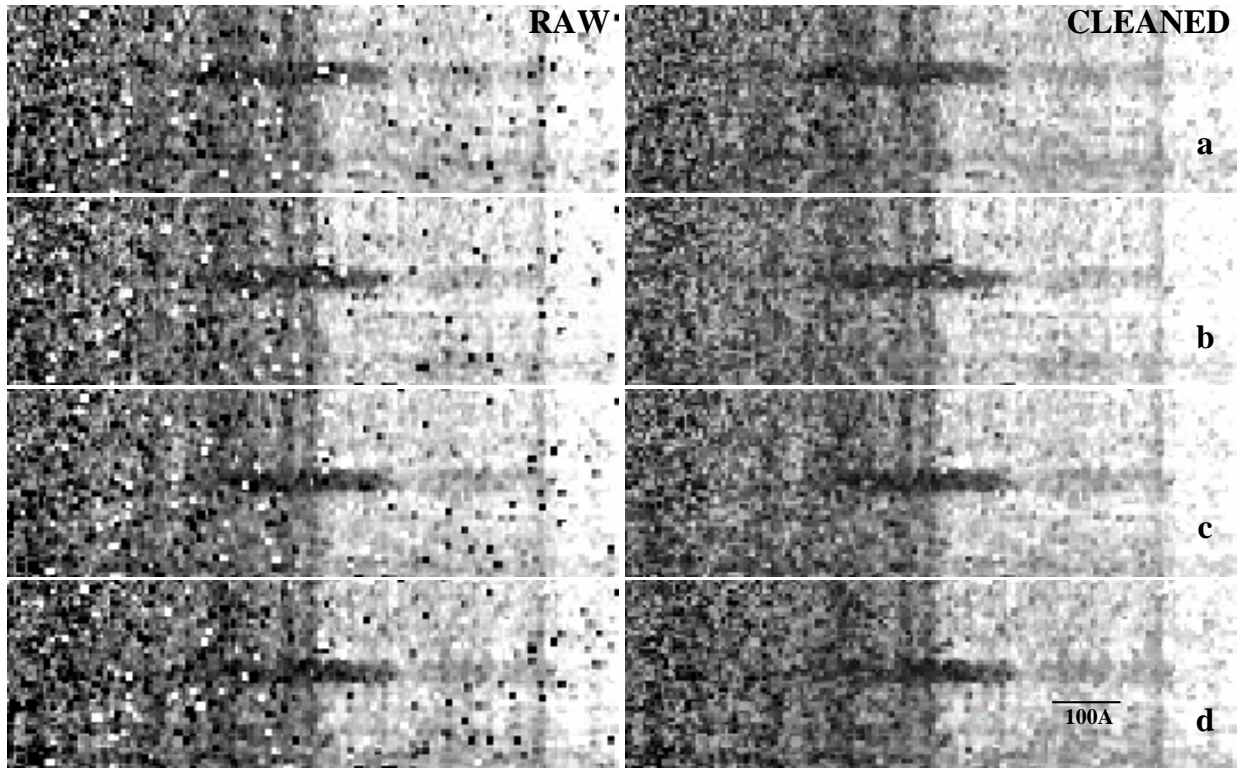


FIG. 4.— The STIS/CCD spectra of SNR 1885 for slit position 2B between 3500 Å and 4500 Å. The dark features are mainly due to Ca II H & K and Ca I 4227 Å absorption. This figure shows an example of hot and cold pixel corrections. *Left*: Raw individual images before pixel corrections. The same portion of the CCD chip is shown in each image. The dithering of SNR 1885 along the slit can be seen as a shift upward along the CCD from bottom to top. *Right*: Individual images post hot and cold pixel correction.

faint signal of SNR 1885 could not be done by simply averaging or summing the dithered observations (see Fig. 5).

In order to correct for these bad pixels, we initially generated a list of bad pixels that differed from their neighboring pixels by a factor of two. These corrections were done only for a  $1''.1$  region surrounding the center of the remnant for each of the observations. The bad pixels were then corrected using the IRAF routine FIX-

PIX, which uses linear interpolation from the neighboring pixels. However, this procedure was viewed as too subjective and did not correct hot and cold pixels in the bulge spectrum immediately surrounding the remnant.

Instead, we adopted a procedure where a mask of bad pixels generated by setting a range of acceptable flux values creating a list of pixels that exceeded this range. Because the flux of the bulge and the sensitivity of the CCD varied significantly between the red and blue wavelengths

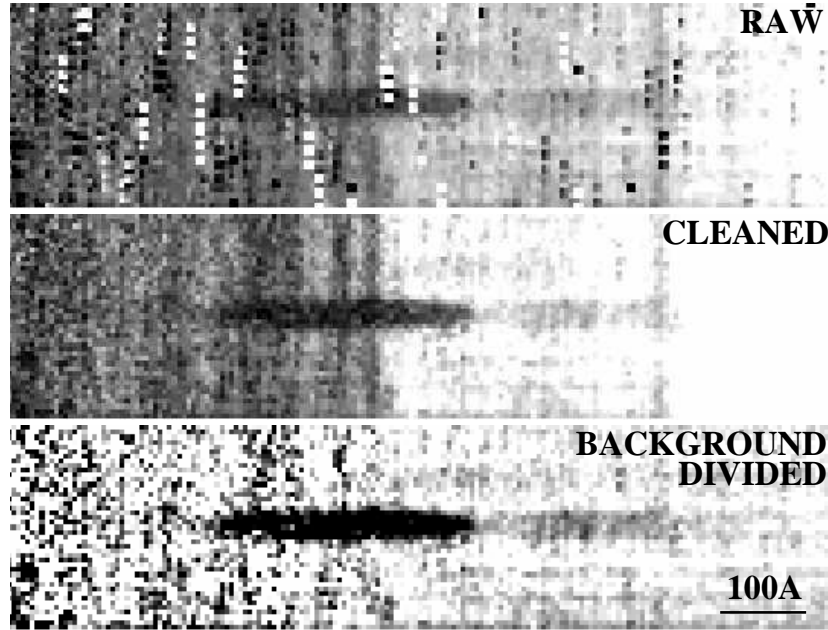


FIG. 5.— *Top*: Raw co-aligned STIS/CCD spectra for slit position 2B. *Middle*: Co-aligned averaged STIS/CCD spectra after hot/cold pixel corrections. *Bottom*: STIS/CCD spectra after removal of M31's bulge spectrum.

TABLE 1  
STIS OBSERVATIONS

Detector	Observation Date	Slit Position
CCD	2013 October 27	1B
CCD	2013 October 21	2B
CCD	2013 October 26	3B
CCD	2013 December 23	1A
CCD	2013 December 09	2A
CCD	2013 December 10	3A
MAMA	2013 December 26	...
MAMA	2013 December 30	...
MAMA	2014 January 02	...

ends covered in the STIS spectra, acceptable ranges were determined in narrow wavelength bins across the spectrum. Using the IRAF task IMREPLACE, the values of bad pixels were replaced with a value equal to 1. The IRAF task IMEXPR was used to create a mask list of bad pixels. This pixel mask was then used as input for FIXPIX and the bad pixels were replaced using linear interpolation of neighboring pixels. An example of this procedure for one slit position is shown in Figure 4, where the left side corresponds to the raw images and the right side corresponds to the cleaned images after pixel corrections.

Following these corrections, individual orbit images were flux scaled using continuum flux values to correct for overall observed flux differences between the orbits. Images were then co-aligned and averaged to form a 2D spectrum at each slit position (see middle panel of Fig. 5).

Because SNR 1885 is detected in absorption against the bulge of M31, the STIS/CCD spectrum contains both SNR 1885's intrinsic spectrum and M31's bulge spectrum. Thus to extract SNR 1885's spectrum, the background consisting of M31's bulge spectrum must be removed.

A STIS/CCD spectrum of M31's bulge was generated using the spectra surrounding the remnant in each of the 24 orbits. Ten  $0''.9$  wide regions were extracted from above and below the remnant in each of the 24 orbits and averaged together to form a single  $0''.9$  average spectrum for each observing direction. These two images were then flux scaled and averaged together to form a single  $0''.9$  image of the M31 bulge spectra. Finally, this  $0''.9$  bulge spectra was averaged together to form the final 1D M31 bulge spectrum seen in Figure 6.

Using this 1D bulge spectrum of M31, we divided the remnant's spectrum by the bulge spectrum to create a fully corrected spectrum of SNR 1885. The final 2D spectra post background division is shown in the bottom panel of Figure 5. This data reduction procedure was applied to all slit positions. The resulting 2D spectra are seen in Figure 7 with the rest wavelengths of Ca I 4227 Å, Ca II H & K, and Fe I 3720 Å labeled.

For each slit position, a single 1D spectrum was created using only the center  $0''.3$  region of the remnant since it contained the highest signal to noise and avoided contamination from the surrounding background region. The 1D spectra from all six slit positions are shown in Figure 8.

### 2.3. STIS/NUV-MAMA Data Reduction

The STIS/NUV-MAMA observations of SNR 1885 were taken at a single slit position across the source but with the source dithered along the detector. This observing configuration allowed us to co-align all the orbits and sum them to form a 2D spectrum of SNR 1885 in the NUV. This spectrum again contains both the remnant's spectrum and the spectrum of M31's bulge.

As done for the STIS/CCD data, M31's bulge spectrum was found using the spectra surrounding the remnant in the summed 2D spectrum. Fifteen  $1''.23$  regions were extracted from above and below the remnant and averaged together to form a single  $1''.23$  average spec-

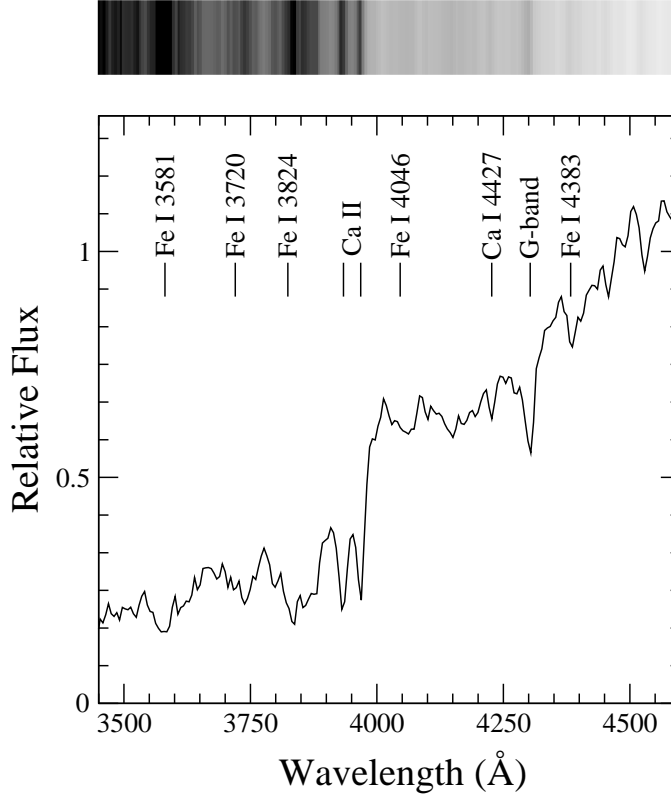


FIG. 6.— *Top*: The STIS/CCD spectrum of the bulge of M31 extracted from all slit positions. This spectra is the final 1D spectrum replicated to fill the 2D array which is then divided into SNR 1885’s spectrum. *Bottom*: The 1D STIS/CCD spectrum of the bulge of M31, with labeled absorption features.

trum. The individual pixels of this 2D image were then averaged to form a single 1D bulge spectrum for M31.

The summed spectrum of SNR 1885 was divided by M31’s bulge spectrum to create a spectrum only containing the remnant’s intrinsic spectrum. The final 2D spectra post background division can be seen in Figure 9.

### 3. RESULTS AND DISCUSSION

#### 3.1. *Ca II H & K*

The goal of taking STIS/CCD observations of SNR 1885 in six separate slit positions was to investigate the three dimensional structure of Ca II absorption across the remnant. Variations in Ca II absorption could indicate regions of increased or decreased  $\text{Ca}^+$  concentrations like those seen in prior narrow passband *HST* Ca II images (Fesen et al. 2007, 2015). However, seeing such variations is difficult even with high signal-to-noise data since the remnant’s Ca II H & K line absorption blend is highly saturated.

The fairly noisy data of the STIS/CCD spectra added to the difficulty in detecting significant variations in the Ca II line profile. Furthermore, at  $\lambda \sim 4000 \text{ \AA}$ , the STIS/CCD spectrograph has a resolution of  $400 \text{ km s}^{-1}$  which limits the determination the radial velocities from the spectra. Due to the high velocities of the Ca I and Ca II in the remnant, there is an overlap between the two absorption features causing an additional limitation in determining the maximum radial velocities observed for Ca II.

Despite these issues, variations of the strength of

the remnant’s Ca II absorption can be clearly seen in the STIS spectra. Figure 7 shows the 2D spectra of SNR 1885 at each of the six slit positions across the remnant. Orientation B shows broader absorption features overall compared to Orientation A. In addition, Orientation B shows more saturated absorption than Orientation A.

The center slit, 2B, shows deep absorption of Ca II 3934, 3968  $\text{\AA}$  extending to 4100  $\text{\AA}$  ( $10\,000 \text{ km s}^{-1}$ ) on the red side and 3790  $\text{\AA}$  ( $11\,000 \text{ km s}^{-1}$ ) on the blue side. For comparison, in center slit 2A, the Ca II extends 4100  $\text{\AA}$  on the red side and 3850  $\text{\AA}$  on the blue side. For slit position 2B, the most extended Ca II features appear in the central region of the remnant along the slit, whereas for slit position 2A, the blue side is most extended near the top of the remnant while the red side appears to be more extended on the bottom. Determining the edges of the Ca II is difficult in the 2D spectra because the Ca II overlaps with the broad Ca I feature on the red side and with Fe I on the blue side.

For data taken in Orientation A, both off center slit positions show a narrower Ca II absorption feature compared to that of the central slit. Slit position 1A, which went through the western portion of the remnant, shows a Ca II absorption feature extending from 3900  $\text{\AA}$  to 4050  $\text{\AA}$ . The Ca II extends furthest in the middle of the slit position 1A’s spectrum and there is a separation between the Ca II and Ca I. For slit position 3A, which went through the eastern portion of the remnant, the Ca II absorption extends from 3960  $\text{\AA}$  to 4100  $\text{\AA}$ . The

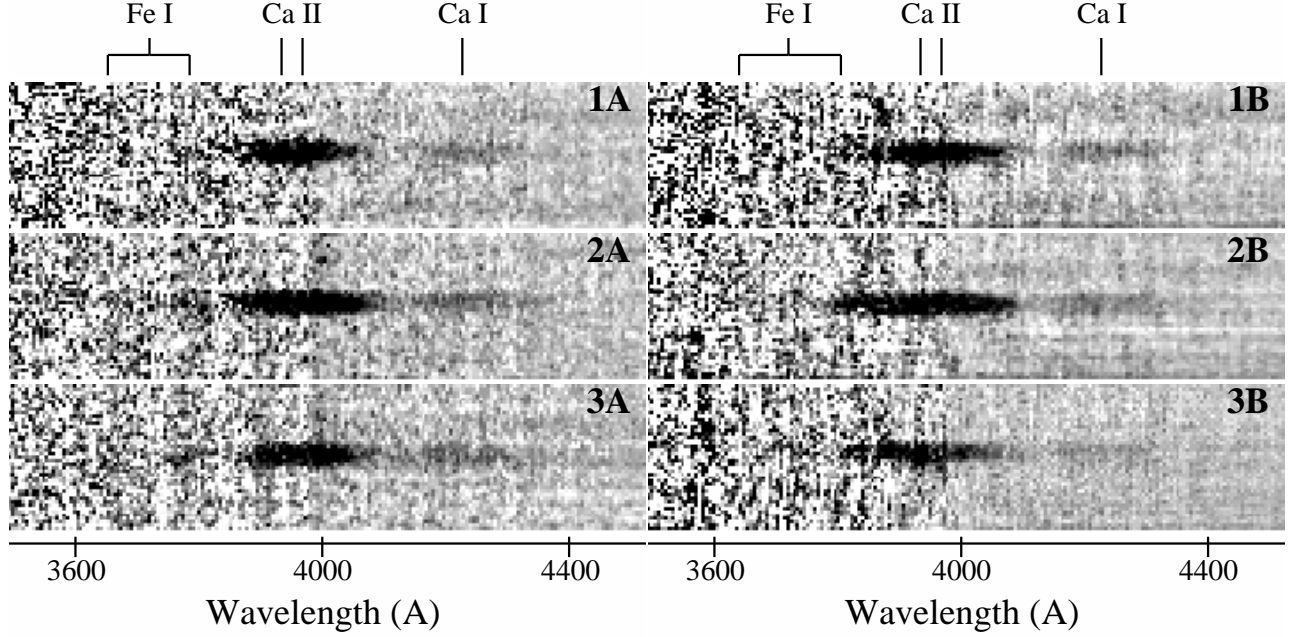


FIG. 7.— Reduced 2D STIS/CCD spectra for SNR 1885 at each of the six slit position. The rest wavelengths of Ca II H & K, and Ca I absorption lines are labeled. The Fe I absorption is labeled according to the observed wavelengths of the shell seen in the 1D spectra. The slit positions noted in the top right correspond to the slit positions shown in Figure 3.

TABLE 2  
VELOCITIES OF ABSORPTION FEATURES DETERMINED FROM 1D STIS/CCD SPECTRA

Slit Position	Ca II		Ca I		Fe I (Blue)		Fe I (Red)	
	Wavelength (Å)	Velocity (km s <sup>-1</sup> )	Wavelength (Å)	Velocity (km s <sup>-1</sup> )	Wavelength (Å)	Velocity (km s <sup>-1</sup> )	Wavelength (Å)	Velocity (km s <sup>-1</sup> )
(1)	(2)	(3)	(4)	(5)	(6)	(7)	(8)	(9)
1A	3830–4105	–8100, +10400	4115–4385	–7700, +11400	3630–3995	–7200, –2100	3750–3810	+2500, +7300
2A	3835–4105	–7700, +10400	4120–4380	–7600, +10900	3610–3695	–9000, –2100	3750–3820	+2400, +8000
3A	3860–4115	–5600, +11100	4115–4375	–8000, +10500	...	...	3735–3830	+1300, +8700
1B	3840–4120	–7200, +11300	4120–4345	–7600, +11300	3625–3700	–7800, –1700	3770–3840	+2400, +9800
2B	3790–4100	–11100, +10000	4100–4400	–9400, +12400	3600–3685	–9000, –2900	3720–3790	~ 0, ≥ 5500
3B	3800–4125	–10000, +11900	4125–4310	–7200, +5800	3645–3705	–6000, –1100	3720–3790	~ 0, +5500

NOTE. — Columns: (1) – Slit positions as labeled in Figure 3. (2 & 3) – Wavelength and velocity of the width of the Ca II absorption feature. The wavelengths and velocities are underestimates of the maximum wavelengths and velocities due to the overlap between the Ca I 4227 Å and Fe I 3720 Å absorption features. (4 & 5) – Wavelength and velocity of the width of the Ca I 4227 Å absorption feature. The blue wavelengths and velocities are underestimates of the maximum wavelength and velocity due to the overlap with the Ca II absorption. The red wavelengths should be a true measure of the maximum radial velocity with the error of the noise. (6 & 7) – Wavelength and velocity of the width of the blue side of the shell of Fe I 3720 Å. (8 & 9) – Wavelength and velocity of the width of the red side of the shell of Fe I 3720 Å. The wavelengths and velocities on the red side of this feature may be underestimates of the true maximum velocity due to the overlap with the blue side of the Ca II absorption.

blue side of the Ca II appears to have a sharp, well defined edge unlike slit positions 1A or 2A. On the red side of the remnant, the edge is not as well defined, as the Ca II overlaps with the Ca I absorption.

In Orientation B, the off center slit positions show narrower and less saturated Ca II absorption compared to that of the central slit. For slit position 1B, which went through the northern portion of the remnant, the Ca II feature extends from 3840 Å to 4120 Å. On the red side of the Ca II absorption, the feature appears asymmet-

ric with deeper absorption near the top of the remnant along the slit. There does not appear to be a separation between the Ca II and Ca I absorption features. However, the depth of the absorption in the overlap region is weaker compared to the central slit. For slit position 3B, which went through the southern portion of the remnant, the Ca II feature extends from 3800 Å to 4125 Å. The blue side of the Ca II feature is noisy, and is most extended through the central region of the remnant along the slit.



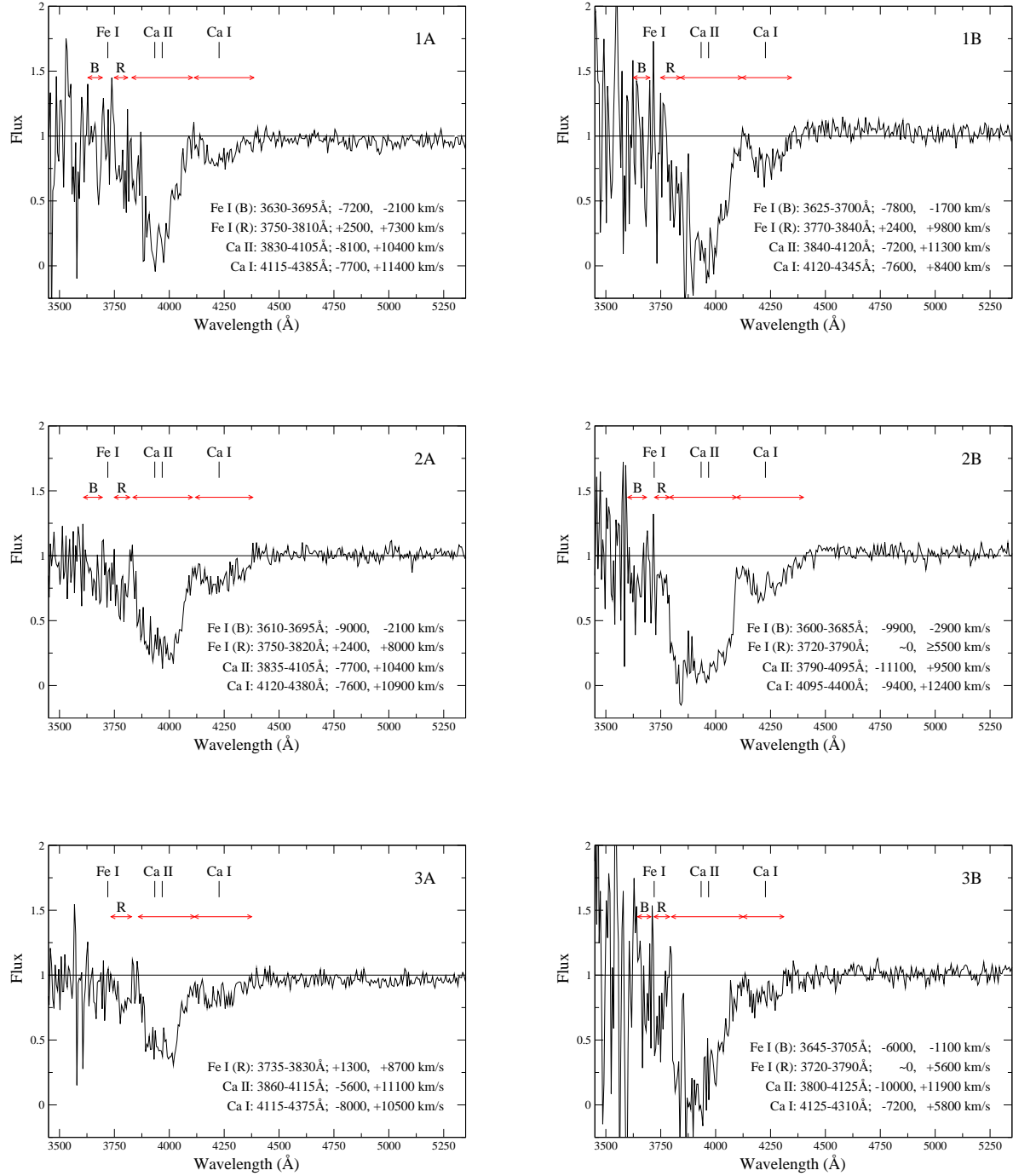


FIG. 8.— The STIS/CCD spectrum for center 0.3 arcseconds for each slit position. The rest wavelengths of Fe I, Ca II H & K, and Ca I absorption lines are labeled. The red lines with arrows correspond to the best approximation of the width of the absorption features for each spectrum. The wavelengths and velocities corresponding to the width of the absorption features are listed in the bottom right. The slit positions noted in the top right of each spectrum corresponds to the slit positions shown in Figure 3.



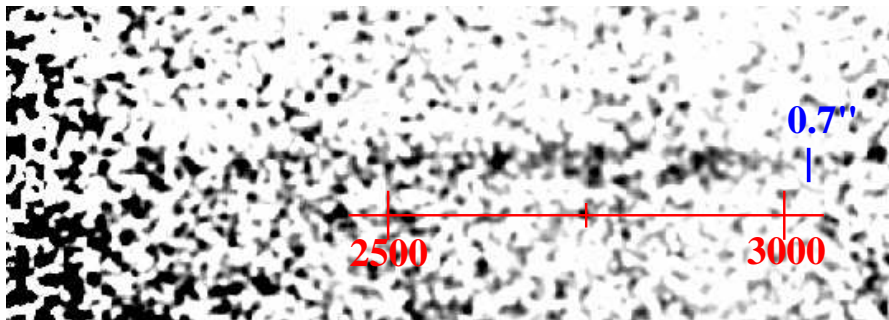


FIG. 9.— Reduced 2D STIS/NUV-MAMA spectra for SNR 1885. The 0.7 arcsecond size of the remnant is noted on the right side of the image in blue. The wavelength scale is given below the remnant in red.

Figure 8 shows 1D spectra of SNR 1885 taken from the center  $0''.3$  through the remnant at each of the six slit positions. All of the 1D spectra show that the Ca II and Ca I absorptions overlap, as the flux on the red side of the feature does not return to the continuum value. This overlap makes it difficult to determine the maximum radial velocity of the Ca II and Ca I in the remnant. The 1D spectra show that for slit position 2B Ca II extends to at least  $4100 \text{ \AA}$  ( $9500 \text{ km s}^{-1}$ ) on the red side and  $3790 \text{ \AA}$  ( $-11\,100 \text{ km s}^{-1}$ ). Similarly, slit position 2A has Ca II on the red side extending to at least  $4105 \text{ \AA}$  ( $10\,400 \text{ km s}^{-1}$ ) and on the blue side extending to  $3835 \text{ \AA}$  ( $-7700 \text{ km s}^{-1}$ ).

### 3.1.1. Changes Between 1996 and 2013

In 1996, a spectrum of SNR 1885 was obtained with the FOS using a  $0''.43$  diameter aperture, and showed strong symmetric Ca II absorption, redshifted Ca I  $4227 \text{ \AA}$  absorption, and strong Fe I  $3720 \text{ \AA}$  absorption (Fesen et al. 1999). This spectrum is reproduced in the bottom panel right panel of Figure 10 for comparison to the STIS/CCD spectra taken in the center two slit positions.

In the 1996 FOS spectrum, the Ca II has a relative flux of approximately 0.25, while the STIS spectrum taken at slit position 2B suggests a significant increase in Ca II absorption especially at negative radial velocities over the last 17 years. However, the spectrum for slit position 2A indicates virtually no increase in relative strength of the Ca II absorption.

The differences in the relative intensity of the Ca II absorption features between Orientations A and B are shown in Figure 10. The apparent differences between the new STIS spectra and the previous FOS spectrum may have more to do with the larger FOS aperture sampling more of the remnant than the narrow STIS slit spectra than real changes in the Ca II during the last two decades.

Interestingly, however, the shape of the Ca II absorption feature does appear to have changed over the past 17 years. In the 1996 FOS spectrum, the Ca II feature appears symmetric on both red and blue sides, while in the STIS/CCD spectra the feature has a steep decrease on the red side and a more gradual decrease on the blue side. This difference in slope suggests that there is currently a higher density of Ca II on the far side of the remnant.

### 3.1.2. A Ca II Shell

Figure 11 shows contour plots of the relative intensity of the redshifted (far-side) Ca II feature as a function of

radial velocity and relative position in the remnant for each of the six slit positions. The Ca II absorption can be seen to extend to at least  $\sim 10\,000 \text{ km s}^{-1}$ . Since the Ca II absorption feature overlaps with the Ca I feature, the Ca II feature on the red side does not return the continuum flux value, and the maximum contour value corresponds to the flux in the overlapping region rather than the continuum. As such the contour plots are not good indicators for the location of the highest velocity Ca II, but can serve as good indicators of the variations in Ca II absorption at low velocity.

Across nearly all slit positions, there is an increased Ca II absorption, seen as dark contours in Figure 11, between  $2000 \text{ km s}^{-1}$  and  $6000 \text{ km s}^{-1}$  indicative of a shell of higher density Ca II on the far side of the remnant. This increase in absorption is seen as a shell in the 2004 *HST* WFC Ca II image adapted from Fesen et al. (2007) (see Fig. 12). The increased absorption is located  $0''.2$  from the center of the remnant, corresponding to a velocity of  $4700 \text{ km s}^{-1}$ . This implies that the Ca II is not uniformly distributed throughout the remnant, but instead has clumps of higher density within a thick shell.

### 3.1.3. Expansion Asymmetry

Deep Ca II images of SNR 1885 show it to have a diameter  $\simeq 0''.8$  (see Fig. 12). This corresponds to undecelerated Ca II-rich debris traveling at a rate of  $12\,500 \text{ km s}^{-1}$  in the plane of the sky. In the STIS/CCD spectra, we measure a maximum radial velocity of  $11\,900 \text{ km s}^{-1}$  in slit position 3B. (Note: In the two center slits the maximum measured radial velocity of the Ca II is  $10\,400 \text{ km s}^{-1}$  (2A) and  $-11\,100 \text{ km s}^{-1}$  (2B).)

Transverse velocity measures the expansion in the plane of the sky, while the radial velocity measures the expansion along the sight. There is a  $\sim 5\%$  difference between the maximum radial velocity measured in the STIS/CCD spectra ( $11\,900 \text{ km s}^{-1}$ ) and the transverse velocity determined from the *HST* Ca II image ( $12\,500 \text{ km s}^{-1}$ ). Since the Ca II absorption in the STIS/CCD spectra overlaps with Ca I and Fe I absorptions, the radial velocities are likely underestimates of the true maximum radial velocity of the Ca II. For comparison, the radial velocity determined from spectral line fitting of the 1996 FOS spectra was  $\sim 13\,000 \text{ km s}^{-1}$  (Fesen et al. 1999).

Differences in the radial and transverse velocities could imply that the ejecta is not expanding freely, or that the remnant's expansion as measured by Ca-rich debris is not perfectly symmetric. The remnant lies within the bulge

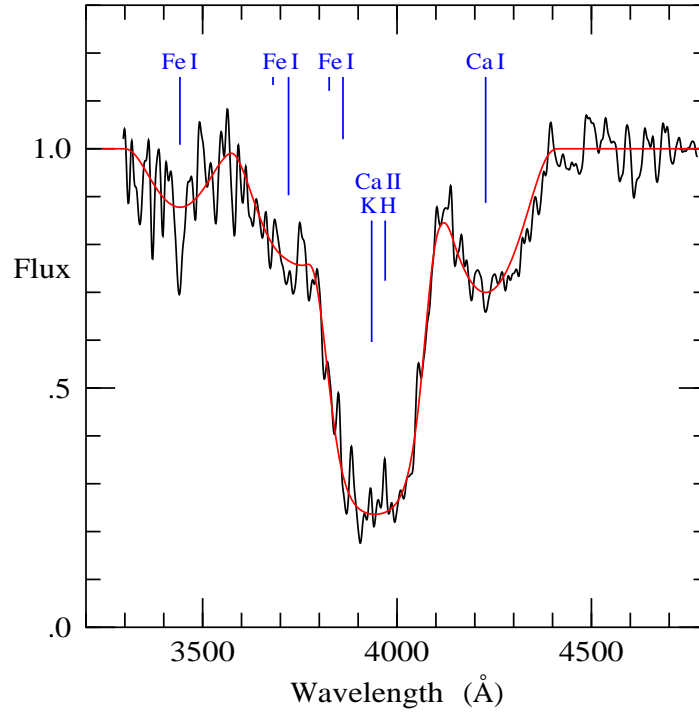
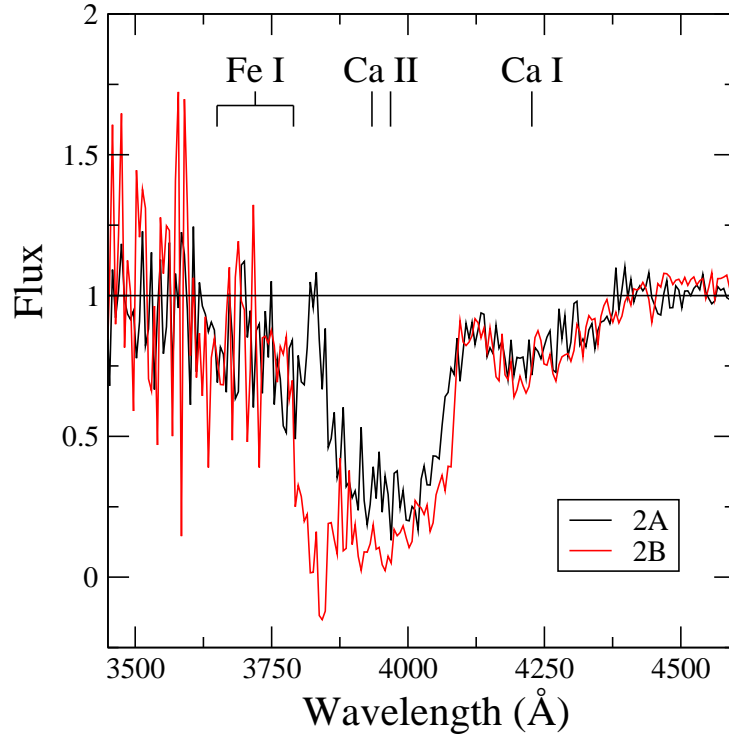


FIG. 10.— *Top*: Overlay of 1D spectra for center 0.3 arcseconds from slit positions 2A and 2B. *Bottom*: 1996 FOS spectrum of SNR 1885 reproduced from Fesen et al. (1999).

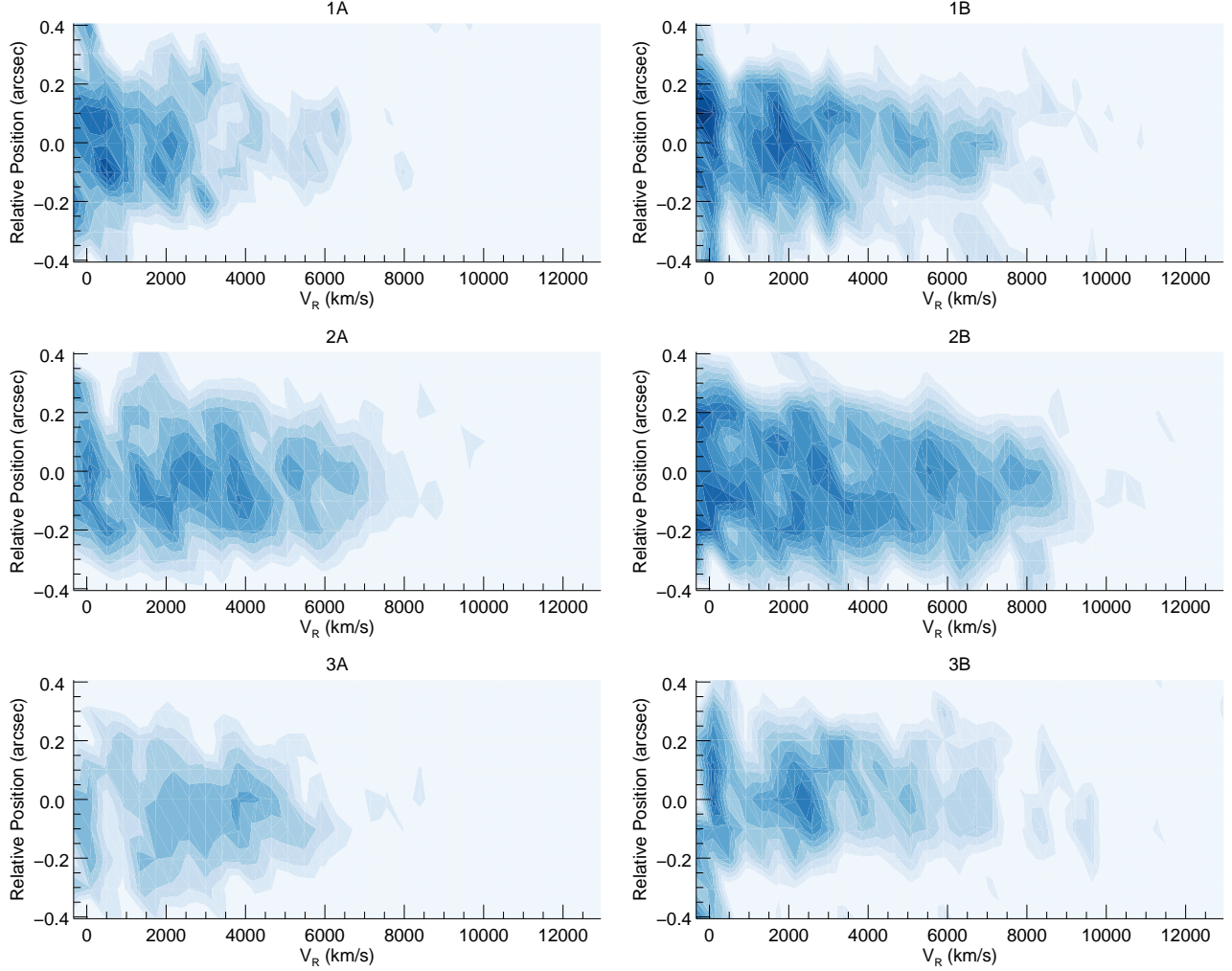


FIG. 11.— Contour plots of the redshifted (far-side) Ca II absorption of SNR 1885. The relative position in arcseconds is determined from the center of the 2D spectra at each of the slit positions. The radial velocity is calculated relative to the Ca II line at 3968 Å. The slit positions noted at the top of each contour plot correspond to the slit positions shown in Figure 3.

of M31 where there are other stars in various evolutionary phases hence could be colliding with material given off by bulge stars as they evolve into the red giant phase.

### 3.2. Ca I

For all slit positions in the 2D STIS/CCD spectra shown in Figure 7, there is absorption to the right of the Ca II 3934, 3968 Å feature, which is attributed to Ca I 4227 Å (Fesen et al. 1999). From our 2D spectra, the central slit 2A shows the broadest Ca I absorption from 4120 Å to 4380 Å. The line center of the Ca I feature appears redshifted by some 30 Å (2100 km s<sup>-1</sup>). In addition, the Ca I absorption appears asymmetric, where there is deeper absorption on the blue side of the line center compared to the red. Additionally, the Ca I absorption appears stronger toward the northern portion of the remnant.

For Orientation B there appears to be uniform Ca I absorption along the height of the remnant between 4110 Å and 4350 Å in slit 2B. As seen before in Orientation A, the Ca I absorption feature is stronger on the blue side than the red side suggesting that the blue side has a higher density of Ca I than the red side.

The weakest Ca I absorption appears in the southern (slit 3B) and western (slit 1A) portions of the remnant. Slit position 1B, on the north side of the remnant, has a Ca I feature which is symmetric along the height of the remnant, but again has stronger absorption on the blue side than the red side. Finally, slit position 3A, located on the eastern side of the remnant, has uniform Ca I absorption across the slit centered on the Ca I 4227 Å line.

Comparison of the 2D (Fig. 7) and 1D (Fig. 8) spectra consistently show an asymmetry in the Ca I absorption. For example, the Ca I feature is broader in the 1D spectrum compared to the 2D spectrum for slit position 2B. The Ca I absorption is measured to be between 4100 Å and 4400 Å, corresponding to radial velocities between -9400 km s<sup>-1</sup> and 12 400 km s<sup>-1</sup>. Similarly, in the 1D spectra, for slit position 2A, the Ca I absorption is narrower compared to 2B, spanning between 4120 Å and 4380 Å or -7600 km s<sup>-1</sup> and 10 900 km s<sup>-1</sup>. It is important to note that the velocities on the blue side of the remnant may be underestimates of the true radial velocity because of the overlap between the Ca I and Ca II absorption features.

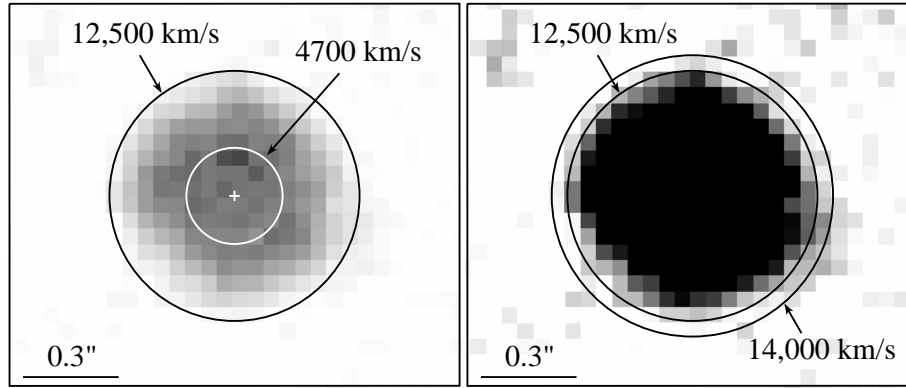


FIG. 12.— The 2004 *HST* ACS WFC Ca II H and K image of SNR 1885. *Left*: The white circle corresponds to the ring of Ca II at a radius  $0''.2$  from the center of the remnant, corresponding to a transverse velocity of  $4700 \text{ km s}^{-1}$ . The outer black circle shown is  $0''.8$  in diameter, corresponding to a transverse velocity of  $12\,500 \text{ km s}^{-1}$ . *Right*: Alternative scaling of the ACS WFC Ca II H and K image of SNR 1885. The inner circle corresponds  $0''.8$  diameter; the size of SNR 1885 as reported by Fesen et al. (2007). The outer circle corresponds to a  $0''.9$  diameter circle which encompasses the extended absorption in the southwest region of the remnant.

Our 1D spectrum for slit position 3B confirms weak Ca I between  $4125 \text{ \AA}$  and  $4310 \text{ \AA}$ . The Ca I absorption feature has a relative flux of  $\approx 0.85$  times the flux of the bulge. For slit position 1A, the Ca I is detected between  $4115 \text{ \AA}$  and  $4385 \text{ \AA}$  with a relative flux of  $\approx 0.8$ . Slit position 3A, has an overall noisy detection of Ca I from its 1D spectrum, between  $4115 \text{ \AA}$  and  $4375 \text{ \AA}$ , at a flux of  $\approx 0.8$  times the flux of the bulge. Ca I was detected in slit 1B between  $4120 \text{ \AA}$  and  $4345 \text{ \AA}$  with a flux of  $\approx 0.8$  times the bulge flux.

Interestingly, from the 1D spectra for all slit positions except 3B, the line center of Ca I feature appears redshifted by  $\sim 1500 \text{ km s}^{-1}$ . Fesen et al. (1999) also reported a redshifted Ca I absorption feature in the FOS spectrum (see Fig. 10), by  $\sim 1100 \text{ km s}^{-1}$ . Fesen et al. (2007) argued that redshifted line center of the Ca I absorption observed in the FOS spectrum could not be accounted for by an anisotropic photoionization model because there should be more ionization on the side closer to the bulge. Anisotropic photoionization would result in an asymmetric Ca I line profile that is blueshifted.

In the 1996 FOS spectrum, the Ca I absorption profile is symmetric about its redshifted line center. However, the 2013 STIS/CCD spectra are asymmetric about their redshifted line center, having decreased flux at high velocity on the red side. This decreased flux at high velocity could be accounted for by an anisotropic photoionization model because the highest velocity Ca I is being ionized more quickly as it is closer to the bulge.

However, an anisotropic photoionization model is not the only possible explanation for the decreased flux at high velocity Ca I. A reverse shock would also diminish the high velocity Ca I, but might similarly affect both the red and blue sides of the remnant. Since the blue side overlaps with Ca II, it is not possible to tell if the blue side also has diminished flux at high velocity, so this explanation cannot be fully investigated. However, the possibility of a strong reverse shock is unlikely as SNR 1885 is an extremely weak radio source (Sjouwerman & Dickel 2001; Hofmann et al. 2013) and there has been no confirmed x-ray emission (Kaaret 2002), which would be expected from an interacting ejecta.

Additionally, the 1D spectra through the center of the remnant for observing Orientation B shows Ca I absorp-

tion on the far side of the remnant out to  $12\,400 \text{ km s}^{-1}$ . This high velocity absorption is not seen for Ca II absorption. The *HST* Ca II image shows some faint, extended absorption in the southwest region of the remnant (see Fig. 12). This extended Ca II absorption has a transverse velocity of approximately  $14\,000 \text{ km s}^{-1}$ .

This extended absorption is only seen in the spectra for slit position 2B suggesting that there are regions with slightly higher expansion velocities. It is not possible to tell if this extension occurs on the near side of the remnant because of the overlap between the Ca I and Ca II absorption features. Furthermore, in the Ca II image the extended absorption only occurs in one region also supporting the notion that the remnant has an asymmetric distribution of Ca. Consequently, it appears clear that any asymmetries in the expansion of SNR 1885 are relatively small.

### 3.3. Fe I

Detection of Fe I  $3720 \text{ \AA}$  was not obvious from the 2D STIS/CCD spectra in Figure 7. The data shortward of  $3800 \text{ \AA}$  is extremely noisy due to the lower background bulge flux and the CCD's lower efficiency at blue wavelengths. However, the average  $0''.3$  spectra from the center regions of each slit (see Fig. 8) provide evidence for a weak detection of Fe I. The center slit positions provide the clearest detection of Fe I at wavelengths blue of  $3720 \text{ \AA}$ , and show that the Fe I absorption is a shell.

In the bottom left panel of Figure 10, which overlays the 1D spectra from the two center slit positions, it is clear that there are two separate absorption features centered about  $\lambda = 3720 \text{ \AA}$ . For slit position 2A, the blue side of Fe I absorption is between  $3610 \text{ \AA}$  ( $-9000 \text{ km s}^{-1}$ ) and  $3695 \text{ \AA}$  ( $-2100 \text{ km s}^{-1}$ ). The red side is between  $3750 \text{ \AA}$  ( $2400 \text{ km s}^{-1}$ ) and  $3820 \text{ \AA}$  ( $8000 \text{ km s}^{-1}$ ).

The blue side of the Fe I absorption feature for slit position 2B is between  $3600 \text{ \AA}$  ( $-9900 \text{ km s}^{-1}$ ) and  $3685 \text{ \AA}$  ( $-2900 \text{ km s}^{-1}$ ). The red side is between  $3720 \text{ \AA}$  ( $\sim 0 \text{ km s}^{-1}$ ) and  $3790 \text{ \AA}$  ( $5500 \text{ km s}^{-1}$ ). For slit position 2B, the red side of the Fe I absorption and blue side of Ca II absorption features overlap, so the maximum radial velocity of the Fe I on the red side may be an underestimate.

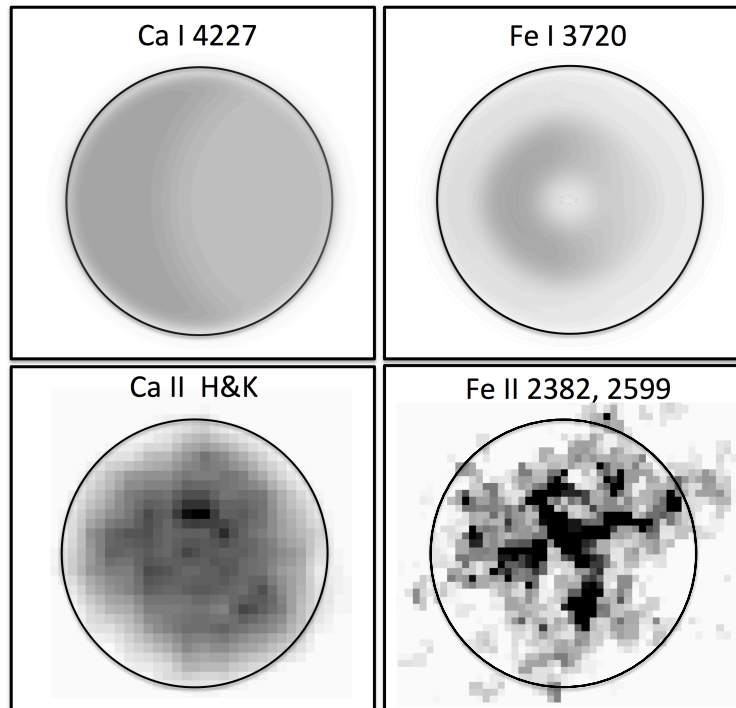


FIG. 13.— Figure showing inferred distributions of Ca I, Ca II, Fe I from this spectral study along with the 2D distribution of Fe II as seen in *HST* imaging (Fesen et al. 2015). The circles (radius =  $0.40''$ ) correspond to an average expansion velocity of  $12\,500\text{ km s}^{-1}$ .

Compared to the 1996 FOS spectrum, the STIS/CCD spectra have a weak detection of Fe I  $3720\text{ \AA}$ . In the FOS spectra, the blue side of the bell shaped Fe I absorption is seen, while the red side overlaps with Ca II. There is no indication of a shell in the FOS spectra. In the STIS/CCD spectra, the blue side of the Fe I absorption is clearly separated from the red side and bell-shaped absorption is not clear.

The 2009 and 2010 *HST* Fe I images do not indicate that Fe I is in a shell (Fesen et al. 2015). The *HST* Fe I images indicate the Fe I is located in a region approximately  $0''.4$  in diameter offset to the Northeast of the Ca II center by approximately  $0''.1$ . The size of the Fe I in the images indicates that the Fe I extends to a transverse velocity of  $\approx 6000\text{ km s}^{-1}$ . The STIS/CCD spectra and *HST* Fe I images together indicate that the concentration of Fe I in the Northeast region of the remnant is located in a shell.

Furthermore, Fesen et al. (2015) presented *HST* Fe II images that indicate the Fe II is located in finger-like plumes extending out to  $\approx 0''.3$  ( $10\,000\text{ km s}^{-1}$ ). The images also indicate that there is Fe II located outside of the plumes which also extends out to  $10\,000\text{ km s}^{-1}$ . The Fe II images also show higher concentrations of Fe II in the center, with less absorption on the edges. The Fe I velocities found from the STIS/CCD spectra confirm the presence of Fe material at high velocities, although the Fe is still located closer to the center of the remnant than the Ca. Furthermore, the shell structure of Fe I in the spectra is consistent with a region of higher ionization in the center of the remnant, where the Fe would have been located in a higher ionization state.

### 3.4. NUV-MAMA

The STIS/NUV-MAMA observations are presented in Figure 9. The STIS/NUV-MAMA observations are extremely noisy, but show a detection of weak absorption below  $3000\text{ \AA}$ . The predicted UV spectra shown in Figure 2 has highly saturated absorption between  $2500\text{ \AA}$  and  $3000\text{ \AA}$ . Below approximately  $2500\text{ \AA}$ , the STIS/NUV-MAMA observations become overwhelmed by noise and no clear signal can be detected. The STIS/NUV-MAMA absorption is seen across an area of  $0''.7$  consistent with the size of SNR 1885 as determined from previous *HST* images.

Since the bulge flux of M31 is weak in the UV, the signal to noise for the detection of SNR 1885 is extremely low. It is not possible to determine whether certain areas of the remnant have increased concentrations of absorption because the differences in absorption at the level of the noise seen outside the remnant. Additionally, it is not possible to determine which features belong to a given element because the absorption is broad and the model spectra predicted large overlap in absorption between different features.

### 3.5. Comparison to SN Ia Models

Figure 13 shows a summary of derived spatial distributions of Ca I, Ca II, and Fe I in SNR 1885 based on the STIS spectra. Also shown is the 2D distribution of Fe II as shown in Fesen et al. (2015) from *HST* images. Below we discuss our spectral results for S And in light of various classes of explosion models for thermonuclear supernovae. As previously suggested, one likely mech-



anism for SNe Ia is the explosion of off-center delayed-detonation model for a WD close to  $M_{Ch}$ .

Within the DDT scenario, most of the C/O WD is burned and thus the explosion energies and the density and velocity structures are similar over a wide range of brightness (Höflich et al. 2002). Which elements are produced depend mostly on the competition between expansion and nuclear burning, and at high temperatures and densities nuclear statistical equilibrium (NSE). While expansion timescales,  $\approx 1$ s, are controlled by hydrodynamics, nuclear burning timescales and NSE are dominated by the temperature under which burning takes place which is a function of the amount of fuel per volume, i.e., the density under which burning takes place.

For C/O mixtures, Ca is produced in a density range between  $\approx 1.5 \times 10^7$  and  $\approx 5 \times 10^6$  g cm $^{-3}$ . At higher densities, Ca is destroyed due to the shift toward NSE. At the inner edge of this density range, Ca is produced during the deflagration phase whereas at the outer edge Ca production is governed by the detonation phase of burning. The size of the Ca-hole depends mostly on the initial central density of the exploding WD and, thus, the WD mass (Höflich et al. 1998; Diamond et al. 2015). To be consistent with a minimum Ca velocity of 2000 km s $^{-1}$  as seen in S And,  $M_{WD}$  must be close (within  $\sim 0.05 M_{\odot}$ ) to  $M_{Ch}$ . This is an lower limit set by mixing. For Branch-normal SNe Ia within the DDT scenario and with suppressed mixing, the total  $^{56}\text{Ni}$  production and the outer edge of Ca both depend the DDT transition. As discussed in Fesen et al. (2007), the brightness of SN 1885 is consistent with the maximum Ca velocity observed, suggesting the inner edge of Ca is insensitive on SN brightness.

Our STIS optical spectra of SNR 1885 show no evidence for extensive mixing as would be expected in a deflagration explosion. The fairly restricted expansion velocities for Ca and Fe-rich ejecta are consistent with previous analyzes which suggested a  $M_{Ch}$  mass model with an off-center, deflagration to detonation transition at the lower end of ‘Branch-normal’ SNe Ia like that of SN 1986g.

Specifically, we find Ca-rich material to be mainly concentrated in a shell of intermediate expansion velocities. This is in contrast to *HST* Fe II images which show a central Fe-rich region plus only a handful of Fe-rich plumes extending out to the edge of the Ca-rich region. Such a layered structure supports the picture of a delayed-detonation transition explosion along with a clumpy structure typical of R-T instabilities during the initial deflagration phase. The degree of Ca and Fe mixing appears greatly suppressed compared to expectations from 3D hydro calculations which would be expected to mix the remnant’s entire central region (Gamezo et al. 2003; Reinecke et al. 2002; Röpke et al. 2012). One possible mechanism for R-T suppression is high magnetic fields (Höflich et al. 2013; Penney et al. 2014; Diamond et al. 2015).

Given the diversity of thermonuclear supernovae and the uncertainties in light curves of SN 1885, there is a wide range of possible explosion mechanisms for S And. Briefly these are: (1) Chandrasekhar mass  $M_{Ch}$  models where the explosion is triggered by compressional heat close to the center when the WD ap-

proaches  $M_{Ch}$ , (2) An explosion triggered by heat released during the dynamical merging or collisions two WDs and (3) A double detonation He-detonation scenario where a C/O WD star accretes He-rich material at a low rate to prevent burning and the explosion is triggered from ignition of the surface He layer which generates a shock wave leading to the detonation of underlying of C/O (Nomoto 1982; Woosley & Weaver 1994; Höflich & Khokhlov 1996; Kromer et al. 2010).

The observed symmetry in S And’s Ca-rich inner layer and the remnant’s overall uniform expansion velocities do not support a violent merger of WDs. Likewise, the presence of a deflagration phase creating R-T scale clumps would seem to disfavor a double detonation type of event. This leaves the conventional Chandrasekhar mass explosion model. Such a model is consistent with many of S And’s observed properties including its clumpy Ca-rich inner ring caused by high density burning.

In summary, the spectral data presented here show evidence for a detonation phase which includes the layered structure of burning products and a distribution of Ca-rich ejecta concentrated in a shell. The Fe distribution in the inner layers exhibits plumes with a scale height typical for Rayleigh-Taylor (R-T) instabilities in all directions. However, the extend of mixing is significantly lower than expected from pure hydro-simulations. Within the framework of spherical explosions,  $M_{Ch} \approx 1.25 M_{\odot}$  models are suggested based on  $v_{Ca(min)}$  (Höflich & Khokhlov 1996) but the morphology is inconsistent with the structures seen in the S And remnant.

#### 4. CONCLUSIONS

Our 2013 and 2014 STIS spectra provide insight into the three dimensional structure of the S And remnant (SNR 1885). From these data, we obtained the following results:

1) The remnant’s broad Ca II H & K absorption extends out to at least 11 500 km s $^{-1}$  on both the near and far sides, consistent with the remnant’s angular dimensions seen in previous *HST* narrow passband Ca II images of S And. We find enhancements of Ca II absorption between expansion velocities of 2000 and 6000 km s $^{-1}$  suggestive of a clumpy Ca II-rich shell, consistent with prior 2D Ca II images. In addition, the scale of the Ca clumps seen in the direct 2D images matches the observed range of expansion velocities of the Ca clumps.

2) Radial velocities from the STIS spectra together with implied transverse velocities from prior *HST* images for Ca II absorptions differ by only slightly suggesting the remnant’s expansion appears is approximately symmetric in three dimensions. The STIS spectra, when taken together with previous direct *HST* images indicate a remnant with less than a 10% departure from purely spherical expansion.

3) Remarkably, even after nearly 130 years the STIS/CCD spectra indicate that there is still a high concentration of Ca I throughout SNR 1885. We find Ca I 4227 Å absorption extending out to 12 400 km s $^{-1}$ . This absorption is seen to be asymmetric and redshifted toward the bulge  $\approx 1500$  km s $^{-1}$ , consistent with the 1996 FOS spectrum. A decrease in Ca I absorption overall and at high velocity is in agreement with the results predicted by Fesen et al. (1999).

4) The STIS spectra reveal weak Fe I 3720 Å absorption confined to a shell with expansion velocities between 2000 and 9000 km s<sup>-1</sup> on both the near and far sides of the remnant. The fact that this shell starts at approximately 2000 km s<sup>-1</sup> is consistent with Fe II 2D images which show a concentration of Fe II near the remnant's center.

5) UV STIS/MAMA spectra covering 1570 – 3180 Å and taken with a 0''.5 wide slit in only one orientation show weak and broad absorption shortward of 3000 Å consistent with model predictions.

Taken together with previous *HST* images, the new spectra show the remnant of SN 1885 has a layered structure with sharp and well defined Ca-rich outer edge consistent with a delayed detonation phase. The remnant's

clumpy inner Ca-rich shell and only a handful Fe-rich plumes suggest the formation of Rayleigh-Taylor instabilities during an initial deflagration phase although significantly suppressed and of a lower mode than expected from hydrodynamic simulations possibly due to magnetic damping. As a likely scenario, we propose SN 1885 was an off-center, delayed detonation and slightly subluminal SN Ia event similar to SN 1986g.

This research was based on NASA/ESA Hubble Space Telescope program GO-13471 from the Space Telescope Science Institute, which is operated by the Association of Universities for Research in Astronomy, Inc. under NASA contract No. NAS5-26555.

## REFERENCES

- Benz, W., Cameron, A. G. W., Press, W. H., & Bowers, R. L. 1990, *ApJ*, 348, 647
- Bloom, J. S., Kasen, D., Shen, K. J., et al. 2012, *ApJ*, 744, L17
- Branch, D., Livio, M., Yungelson, L. R., Boffi, F. R., & Baron, E. 1995, *PASP*, 107, 1019
- Burstein, D., Bertola, F., Buson, L. M., Faber, S. M., & Lauer, T. R. 1988, *ApJ*, 328, 440
- Chevalier, R. A., & Plait, P. C. 1988, *ApJ*, 331, L109
- Colgate, S. A., & McKee, C. 1969, *ApJ*, 157, 623
- de Vaucouleurs, G., & Corwin, H. G., Jr. 1985, *ApJ*, 295, 287
- Diamond, T. R., Höflich, P., & Gerardy, C. L. 2015, *ApJ*, 806, 107
- Fesen, R. A., Gerardy, C. L., McLin, K. M., & Hamilton, A. J. S. 1999, *ApJ*, 514, 195
- Fesen, R. A., Höflich, P. A., Hamilton, A. J. S., Hammell, M. C., Gerardy, C. L., Khokhlov, A. M., & Wheeler, J. C. 2007, *ApJ*, 658, 396
- Fesen, R. A., Höflich, P. A., & Hamilton, A. J. S. 2015, *ApJ*, 804, 140
- Fesen, R. A., Saken, J. M., & Hamilton, A. J. S. 1989, *ApJ*, 341, L55
- Foley, R. J., Challis, P., Chornock, R., et al. 2013, *ApJ*, 767, 57
- Gamezo, V. N., Khokhlov, A. M., Oran, E. S., Chitchekanova, A. Y., & Rosenberg, R. O. 2003, *Science*, 299, 77
- Gamezo, V. N., Khokhlov, A. M., & Oran, E. S. 2004, *Physical Review Letters*, 92, 211102
- Gamezo, V. N., Khokhlov, A. M., & Oran, E. S. 2005, *ApJ*, 623, 337
- Garcia-Senz, D., & Woosley, S. E. 1995, *ApJ*, 454, 895
- Hamilton, A. J. S., & Fesen, R. A. 1991, in *Supernovae*, 10th Santa Cruz Summer Workshop in Astronomy and Astrophysics, ed. S. E. Woosley (Berlin: Springer-Verlag), 656
- Hamilton, A. J. S., & Fesen, R. A. 2000, *ApJ*, 542, 779
- Hillebrandt, W., Kromer, M., Röpke, F. K., & Ruiter, A. J. 2013, *Frontiers of Physics*, 8, 116
- Hillebrandt, W., & Niemeyer, J. C. 2000, *ARA&A*, 38, 191
- Höflich, P., Gerardy, C. L., Fesen, R. A., & Sakai, S. 2002, *ApJ*, 568, 791
- Höflich, P., Khokhlov, A. 1996, *ApJ*, 457, 500
- Höflich, P., Wheeler, J. C., and Thielemann, F.K. 1998, *ApJ*, 495, 617
- Höflich, P., Gerardy, C. L., Nomoto, K., Motohara, K., Fesen, R. A., Maeda, K., Ohkubo, T., & Tominaga, N. 2004, *ApJ*, 617, 1258
- Höflich, P., Dragulin, P., Mitchell, J., Penney, B., Sadler, B., Diamond, T., Gerardy, C. 2013, *Frontiers of Physics*, 8, 144
- Höflich, P., Khokhlov, A., Wheeler, J.C. 1995, *ApJ*, 444, 211
- Höflich, P., Wheeler, J. C., & Thielemann, F. K. 1998, *ApJ*, 495, 617
- Höflich, P., & Stein, J. 2002, *ApJ*, 568, 771
- Hofmann, F., Pietsch, W., Henze, M., et al. 2013, *A&A*, 555, A65
- Howell, D. A. 2011, *Nature Communications*, 2, 350
- Hoyle, F., & Fowler, W. A. 1960, *ApJ*, 132, 565
- Iben, I., Jr., & Tutukov, A. V. 1984, *ApJS*, 54, 335
- Isern, J., Hernanz, M., & José, J. 2011, *Lecture Notes in Physics*, Berlin Springer Verlag, 812, 233
- Kaaret, P. 2002, *ApJ*, 578, 114
- Khokhlov, A. M. 1991, *A&A*, 245, L25
- Khokhlov, A., Müller, E., & Höflich, P. 1993, *A&A*, 270, 223
- Khokhlov, A. M. 1995, *ApJ*, 449, 695
- Kromer, M., Sim, S. A., Fink, M., et al. 2010, *ApJ*, 719, 1067
- Kromer, M., Fink, M., Stanishev, V., et al. 2013, *MNRAS*, 429, 2287
- Larsson, J., Fransson, C., Kjaer, K., et al. 2013, *ApJ*, 768, 89
- Li, W., Filippenko, A. V., Chornock, R., et al. 2003, *PASP*, 115, 453L
- Li W., Leaman, J., Chornock, R., et al., 2011, *MNRAS*, 412, 1441
- Livne, E. 1999, *ApJ*, 527, L97
- Livne, E., Asida, S. M., Höflich, P. 2005, *ApJ*, 632, 443
- Maeda, K., Taubenberger, S., Sollerman, J., et al. 2010, *ApJ*, 708, 1703
- McConnachie, A. W., Irwin, M. J., Ferguson, A. M. N., et al. 2005, *MNRAS*, 356, 979
- Morton, D. C. 1991, *ApJS*, 77, 119
- Niemeyer, J. C., & Hillebrandt, W. 1995, *ApJ*, 452, 779
- Niemeyer, J. C., Hillebrandt, W., & Woosley, S. E. 1996, *ApJ*, 471, 903
- Nomoto, K. 1982, *ApJ*, 253, 798
- Nomoto, K., Thielemann, F.-K., & Yokoi, K. 1984, *ApJ*, 286, 644
- Nomoto, K., Uenishi, T., Kobayashi, C. et al. 2003, in: *From Twilight to Highlight: The Physics of Supernovae*, p. 115
- Nugent, P. E., Sullivan, M., Cenko, S. B., et al. 2011, *Nature*, 480, 344
- Osterbrock, D. E. 2001, 'Walter Baade A Life in Astrophysics', Donald E. Osterbrock, Princeton, NJ, USA: Princeton University Press. 2001, p. 93
- Pakmor, R., Hachinger, S., Röpke, F. K., & Hillebrandt, W. 2011, *A&A*, 528, A117
- Pastorello, A., et al. 2008, *MNRAS*, 389, 113
- Penney, R., Höflich, P., 2014, *ApJ*, 795, 84
- Reming, I.S., Khokhlov, A.M. 2014, *ApJ*, 794, 87
- Perets, H. B., Badenes, C., Arcavi, I., Simon, J. D., & Gal-yam, A. 2011, *ApJ*, 730, 89
- Plewa, T. 2007, *ApJ*, 657, 942
- Quimby, R., Höflich, P., Kannappan, S. J., et al. 2006, *ApJ*, 636, 400
- Rasio, F. A., & Shapiro, S. L. 1994, *ApJ*, 432, 242
- Reinecke, M., Hillebrandt, W., & Niemeyer, J. C. 1999, *A&A*, 347, 739
- Reinecke, M., Hillebrandt, W., & Niemeyer, J. C. 2002, *A&A*, 391, 1167
- Röpke, F. K., Hillebrandt, W., Niemeyer, J. C., & Woosley, S. E. 2006, *A&A*, 448, 1
- Röpke, F.K., Woosley, S.E., Hillebrandt, W. 2007, *ApJ*, 660, 1344
- Röpke, F.K., Kromer, D., Seitenzahl, I.R. et al. 2012, *ApJ*, 750, L19
- Seitenzahl, I. R., Ciaraldi-Schoolmann, F., Röpke, F. K., et al. 2013, *MNRAS*, 429, 1156
- Sjouwerman, L. O., & Dickel, J. R. 2001, *Young Supernova Remnants*, 565, 433
- Di Stefano, R., Voss, R., & Claeys, J. S. W. 2011, *ApJ*, 738, LL1
- Di Stefano, R., & Kilic, M. 2012, *ApJ*, 759, 56



- Stritzinger, M. D., Hsiao, E., Valenti, S., et al. 2014, *A&A*, 561, AA146
- Sugimoto, D., & Nomoto, K. 1980, *Space Sci. Rev.*, 25, 155
- Timmes, F. X., & Woosley, S. E. 1992, *ApJ*, 396, 649
- Wang, B., & Han, Z. 2012, *New Astronomy*, 56, 122
- Webbink, R. F. 1984, *ApJ*, 277, 355
- Woosley, S. E., & Weaver, T. A. 1994, *ApJ*, 423, 371
- Yamaoka, H., Nomoto, K., Shigeyama, T., & Thielemann, F.-K. 1992, *ApJ*, 393, L55